NeuroImage: Clinical 30 (2021) 102657

Contents lists available at ScienceDirect

NeuroImage: Clinical

journal homepage: www.elsevier.com/locate/ynicl

Quantification of different iron forms in the aceruloplasminemia brain to explore iron-related neurodegeneration

Lena H.P. Vroegindeweij [a,1], Lucia Bossoni [b,1,*], Agnita J.W. Boon [c], J.H. Paul Wilson [a], Marjolein Bulk [b], Jacqueline Labra-Muñoz [d,e], Martina Huber [d], Andrew Webb [b], Louise van der Weerd [b], Janneke G. Langendonk [a]

[a] Department of Internal Medicine, Center for Lysosomal and Metabolic Diseases, Porphyria Center Rotterdam, Erasmus University Medical Center, Erasmus MC, Rotterdam, the Netherlands
[b] C. J. Gorter Center for High Field MRI, Department of Radiology, Leiden University Medical Center, Leiden, the Netherlands
[c] Department of Neurology, Erasmus University Medical Center, Erasmus MC, Rotterdam, the Netherlands
[d] Department of Physics, Huygens-Kamerlingh Onnes Laboratory, Leiden University, Niels Bohrweg 2, 2333CA Leiden, the Netherlands
[e] Kavli Institute of Nanoscience, Delft University of Technology, Lorentzweg 1, 2628 CJ Delft, the Netherlands

ARTICLE INFO

Keywords:
Aceruloplasminemia
Iron
Post-mortem MRI
Ferritin
Magnetometry

ABSTRACT

Aims: Aceruloplasminemia is an ultra-rare neurodegenerative disorder associated with massive brain iron deposits, of which the molecular composition is unknown. We aimed to quantitatively determine the molecular iron forms in the aceruloplasminemia brain, and to illustrate their influence on iron-sensitive MRI metrics.

Methods: The inhomogeneous transverse relaxation rate (R_2*) and magnetic susceptibility obtained from 7 T MRI were combined with Electron Paramagnetic Resonance (EPR) and Superconducting Quantum Interference Device (SQUID) magnetometry. The basal ganglia, thalamus, red nucleus, dentate nucleus, superior- and middle temporal gyrus and white matter of a post-mortem aceruloplasminemia brain were studied. MRI, EPR and SQUID results that had been previously obtained from the temporal cortex of healthy controls were included for comparison.

Results: The brain iron pool in aceruloplasminemia detected in this study consisted of EPR-detectable Fe^{3+} ions, magnetic Fe^{3+} embedded in the core of ferritin and hemosiderin (ferrihydrite-iron), and magnetic Fe^{3+} embedded in oxidized magnetite/maghemite minerals (maghemite-iron). Ferrihydrite-iron represented above 90% of all iron and was the main driver of iron-sensitive MRI contrast. Although deep gray matter structures were three times richer in ferrihydrite-iron than the temporal cortex, ferrihydrite-iron was already six times more abundant in the temporal cortex of the patient with aceruloplasminemia compared to the healthy situation (162 μg/g vs. 27 μg/g), on average. The concentrations of Fe^{3+} ions and maghemite-iron in the temporal cortex in aceruloplasminemia were within the range of those in the control subjects.

Conclusions: Iron-related neurodegeneration in aceruloplasminemia is primarily associated with an increase in ferrihydrite-iron, with ferrihydrite-iron being the major determinant of iron-sensitive MRI contrast.

1. Introduction

Aceruloplasminemia (OMIM #604290) is a severe adult-onset form of Neurodegeneration with Brain Iron Accumulation (NBIA), caused by homozygous or compound heterozygous mutations in the ceruloplasmin (*CP*) gene. Iron accumulation in aceruloplasminemia has been directly linked to its genetic background, as ceruloplasmin-mediated oxidation of ferrous iron (Fe^{2+}) to ferric iron (Fe^{3+}) is a prerequisite for transport of iron across cell membranes and for binding to transferrin (Miyajima et al., 2003). As a result of ceruloplasmin dysfunction in the brain

Abbreviations: NBIA, Neurodegeneration with Brain Iron Accumulation; CP, ceruloplasmin; QSM, Quantitative Susceptibility Mapping; EPR, Electron Paramagnetic Resonance; SQUID, Superconducting Quantum Interference Device; ROI, Region of interest; IRM, Isothermal Remanent Magnetization; SIRM, Saturation Isothermal Remanent Magnetization.

* Corresponding author at: Leiden University Medical Center, PO Box 9600, 2300 RC Leiden, The Netherlands.
E-mail address: l.bossoni@lumc.nl (L. Bossoni).

[1] Both authors contributed equally to the manuscript.

https://doi.org/10.1016/j.nicl.2021.102657
Received 21 December 2020; Received in revised form 24 February 2021; Accepted 30 March 2021
Available online 3 April 2021

leading to insufficient cellular iron efflux, iron accumulates within perivascular astrocytes, with total iron concentrations reaching over 600 μg/g in the basal ganglia (Miyajima, 2015), which is at least five times the normal concentration (Morita et al., 1995; Miyajima, 2015). However, the exact role of different iron forms in the pathophysiology and clinical phenotype of aceruloplasminemia is still not clear. Molecular specification of the massive iron pool in the aceruloplasminemia brain can aid our understanding of iron related neurodegeneration, and perhaps improve therapeutic considerations, which are currently based on iron chelation.

Among the molecular forms in which iron can be found in the brain, three are particularly relevant. In the healthy human brain, iron is predominantly stored within the core of ferritin and hemosiderin, in the form of Fe^{3+}- containing ferrihydrite nanocrystals (Fe_5O_8H) (Sassi and Rosso, 2019; Dobson, 2001). These iron stores are generally regarded as non-damaging and are required for normal brain functions. In contrast, Fe^{2+} ions taking part in the labile iron pool have been associated with iron-related neuronal damage through generation of free radicals via the Fenton reaction (Miyajima et al., 2003; Dobson, 2001; Markesbery, 1997). The iron-oxide magnetite (Fe_3O_4) is a carrier of Fe^{2+} and has been suggested to play a role in iron-related neurodegeneration (Dobson, 2001; Kirschvink et al., 1992). Histochemical studies in aceruloplasminemia have indicated an abundance of ferritin-bound iron (Kaneko et al., 2002, 2012), and smaller amounts of Fe^{2+} carriers (Kaneko et al., 2002; Gonzalez-Cuyar et al., 2008). However, no quantitative studies have been performed to further determine the molecular forms of iron and their distribution throughout the aceruloplasminemia brain.

Iron-sensitive MRI techniques have been commonly applied as an indirect measure of brain iron content in neurodegenerative disorders, using the effect that (para)magnetic iron has on the proton nuclear relaxation rate (R_2*) and on the magnetic susceptibility of the tissue (χ), which can be measured by Quantitative Susceptibility Mapping (QSM) (Haacke et al., 2005; Dusek et al., 2013). Although R_2* mapping is recognized as a robust method to infer iron accumulation in brain tissue, it is affected by several confounders such as cell water content, the macromolecular pool, the degree of myelination and fiber orientation (Cherubini et al., 2009; Wharton and Bowtell, 2012). In particular, myelin and iron have the same effect on R_2* values (Stüber et al., 2014). QSM, on the other hand, has the potential to differentiate between myelin and iron, based on their opposite effects on tissue susceptibility (Gong et al., 2019), and seems less affected by the cellular localization of iron (Colgan et al., 2020). Both iron-sensitive MRI techniques have been used for the quantitative assessment of iron in aceruloplasminemia brain tissue (Pan et al., 2011; Zhou et al., 2020), but only provided indirect information on the total iron concentrations and not their specification (Bulk et al., 2018).

The primary aim of this study was to quantify different molecular iron forms in the aceruloplasminemia brain. For this purpose, we performed Electron Paramagnetic Resonance (EPR) and Superconducting Quantum Interference Device (SQUID) magnetometry on ten brain regions derived from a post-mortem aceruloplasminemia brain. Due to the rarity of the disease, aceruloplasminemia brain material is extremely scarce. We present a quantitative overview of Fe^{3+} ions detected by EPR, and magnetic Fe^{3+} embedded in ferritin cores or hemosiderin (ferrihydrite-iron) and oxidized magnetite/maghemite minerals (maghemite-iron), as detected by magnetometry. R_2* and QSM maps from the same regions are shown with the additional aim to illustrate the extent to which different iron forms affect iron-sensitive MRI metrics. Since MRI is the major imaging modality capable of studying brain iron accumulation *in vivo*, further specification of the molecular basis of iron-sensitive MRI contrast is key to gain more in-depth pathophysiological insights into different clinical stages of iron-related neurodegeneration.

2. Methods

2.1. Brain tissue selection

Formalin-fixed brain slices of one end-stage aceruloplasminemia patient (52 years,male) were obtained from the Department of Pathology, Erasmus University Medical Center, Erasmus MC, Rotterdam, The Netherlands. His neurological phenotype has been previously published, and was characterized by orofacial dyskinesia, chorea, dystonia, dysarthria and a predominantly ataxic gait disturbance (Vroegindeweij et al., 2015, 2017; Kerkhof and Honkoop, 2014). He gradually deteriorated despite combined iron chelation therapy with deferiprone and phlebotomy (Vroegindeweij et al., 2020). He became bedridden and died from bronchopneumonia years after the onset of neurological symptoms. The brain slices had been stored in formalin for 5 years. Tissue blocks of approximately 30 × 30 × 10 mm^3 were dissected, including the basal ganglia, thalamus, red nucleus, dentate nucleus, superior- and middle temporal gyrus and white matter. Ceramic tools were used to prevent metal contamination of the samples. The study was approved by the Medical Ethics Review Board of the Erasmus MC. The patient's legal representative provided written informed consent.

2.2. MRI data acquisition and data analysis

Before MRI, the dissected tissue blocks were rehydrated in phosphate buffered saline (PBS) for 24 h and immersed in a proton-free solution (Fomblin LC08, Solvay). This is known to partially restore the transverse relaxation times, which are typically shortened by fixation (Shepherd et al., 2009). ICP-MS detected iron traces up to 3.5 μg/ml in the formalin solution, likely due to leakage of iron from the tissue over time. MRI scans were performed at room temperature on a 7 T preclinical scanner (Bruker Biospin, Ettlingen, Germany) using a 38-mm quadrature RF coil. The MR acquisition consisted of a three-dimensional multi-gradient-echo sequence with eight equally spaced echoes. First echo-time was 1.96 ms, echo spacing was 2.21 ms, repetition time was 130.4 ms, flip angle was 25°, 150 μm^3 isotropic spatial resolution. 20 averages were acquired. The total acquisition time was 3 h 54 min.

R_2* ($1/T_2$*) maps were obtained by fitting the signal decay of the magnitude images to a mono-exponential decay function, excluding the echoes that hit the noise floor (Bouhrara et al., 2015). The assumption of mono-exponentiality was tested and verified in all tissue blocks. A deviation from mono-exponentiality was observed in a few, regionally aspecific, pixels in the tissue block containing the basal ganglia (Supplementary material, Fig. S1). While the presence of a second component in the echo decay is relevant in the case of a microscopically inhomogeneous distribution of iron forms, given the scarcity of the pixels featuring a bi-exponential decay, and the limited number of echoes over which the fit could be performed, we report here the results of the mono-exponential fit, also for the block containing the basal ganglia. A dominant mono-exponential component hints at the fact that one form of iron may be the main driver of R_2* relaxation.

Susceptibility values (χ) were obtained from the eight-echoes phase images of the multi-gradient-echo data, with the STI-Suite software (version 2.2) (Li et al., 2014). Phase unwrapping of the measured phase images and removal of the background field was done with the iHARPERELLA algorithm (Li et al., 2015), while magnetic susceptibility estimation and streaking artifact correction was performed with the 'iLSQR' algorithm (Li et al., 2015). Raw susceptibility values are reported, as no reference region was available in these small tissue samples. Regions of interest (ROIs) were manually drawn within each deep gray matter region, middle temporal gyrus and temporal white matter. For each ROI, mean R_2* and magnetic susceptibility values were reported.

Additional MR images that had been previously acquired (Bulk et al., 2018) on tissue blocks containing the temporal cortex and the striatum of two control subjects are used as references to illustrate the effect of

iron accumulation in the aceruloplasminimia brain on MRI maps. These control tissue blocks had been scanned with an acquisition protocol as described above, with the exception of the echo timing, which was increased as the iron concentration was much lower in these control cases: the first echo time was 12.5 ms long, and the inter-echo time was 10.7 ms.

2.3. EPR experiments and spectra fitting

After MRI, subsections of approximately 40 mg were taken from each gray and white matter structure in the tissue blocks (Fig. 1). The resulting subsections were prepared for EPR as previously described (Kumar et al., 2016). The 9 GHz continuous wave EPR measurements were performed at 6 K using an ELEXSYS E680 spectrometer (Bruker, Rheinstetten, Germany) equipped with a rectangular cavity. The microwave frequency was 9.4859 GHz, modulation frequency 90 kHz, power attenuation 20 dB, receiver gain 60 dB and modulation amplitude 6 Gpp. Power attenuation was chosen after a progressive power saturation experiment (Supplementary material, Fig. S2). The accumulation time was approximately five minutes per spectrum.

Fig. 2 shows a baseline corrected EPR spectrum of the tissue block extracted from the putamen. While the spectra consisted of several bands, in this work, we focused on the low field g'=4.3 band, which originates from high-spin Fe^{3+} complexed in a site of low symmetry (Kumar et al., 2016). A close look at the temperature dependence of the amplitude band suggests the presence of a weak antiferromagnetic coupling (Supplementary material, Fig. S3).

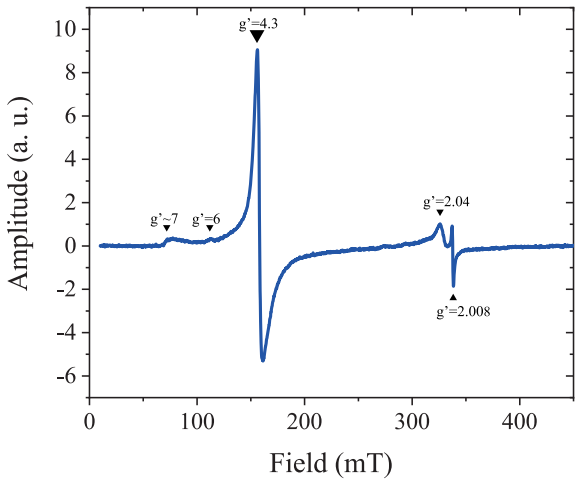

Fig. 2. Determination of Fe^{3+} ions by Electron Paramagnetic Resonance (EPR) at 6 K. First derivative, baseline corrected EPR spectrum of the putamen. The spectrum consists of several bands: a g'~7 poorly defined signal, a weak band at g'=6, an intense band at g'=4.3, a largely asymmetric band around g'=2.04, and a narrow band at g'=2.008.

The g'=4.3 bands detected in each sample were fit to the spin Hamiltonian which describes high-spin Fe^{3+} (Kumar et al., 2016). EPR spectra simulations and fitting were done with EasySpin version 5.2.28

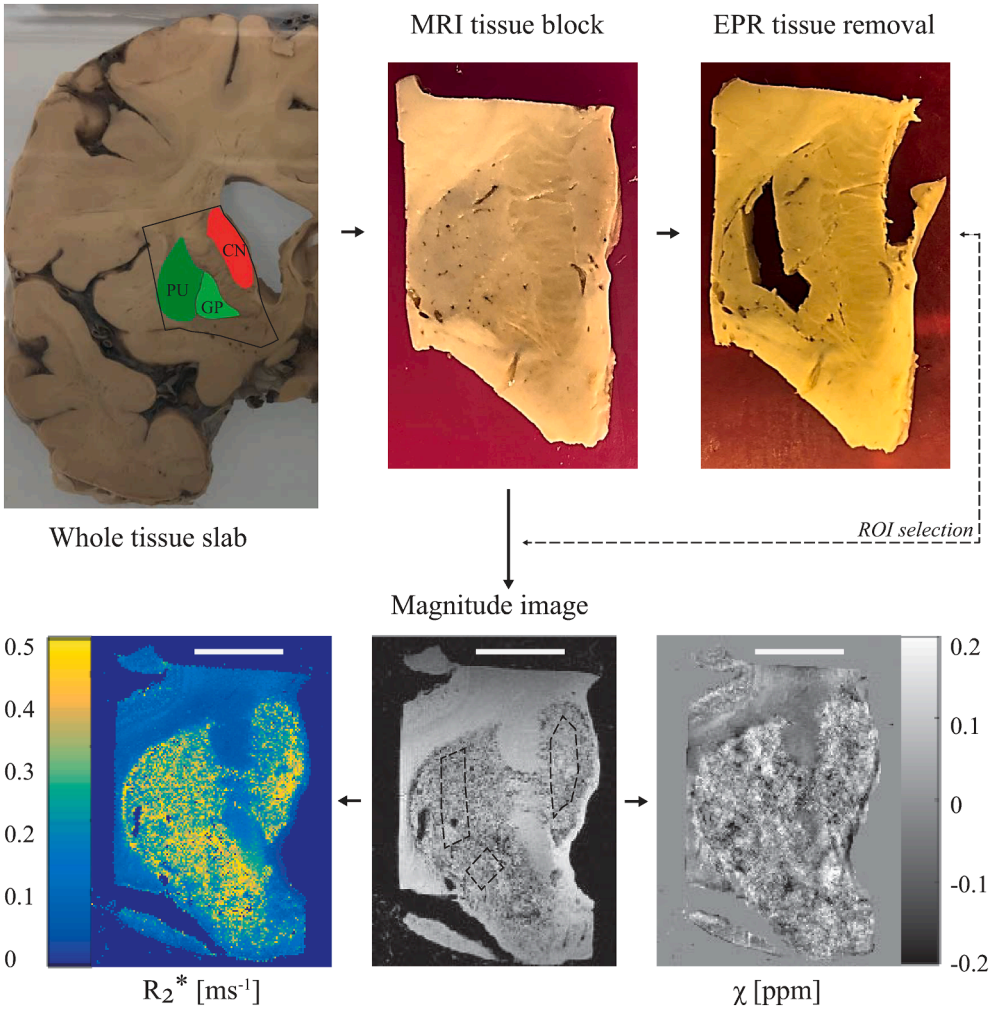

Fig. 1. Pipeline of the experimental protocol. In this example, the basal ganglia (caudate nucleus – CN, putamen – PU, globus pallidus – GP), were dissected from the appropriate brain slab and prepared for MRI. Following MRI, small subsections were taken from each basal ganglia structure and prepared for EPR. Regions of interest (ROIs) on the MRI were matched with the EPR sampling locations. For SQUID, subsections of tissue were taken adjacent to the sampling locations for EPR. Scale bar in the bottom figures, 1 cm.

(Stoll and Schweiger, 2006). Fitting parameters and examples of the fitted spectra are shown in the Supplementary material (Table S1 and Fig. S4). The Fe^{3+} concentration of each sample was calculated by taking the second integral of the fitted spectrum and comparing it to the second integral of a reference solution Fe-EDTA of known Fe^{3+} concentration (35.7 μM).

2.4. Magnetometry experiments

Following EPR experiments, subsections were taken from the caudate nucleus, putamen, substantia nigra, thalamus, red nucleus, dentate nucleus, temporal cortex and white matter, mostly adjacent to the sampling locations for EPR. The total volume of specimens for each brain region was approximately $10 \times 10 \times 10$ mm^3. The globus pallidus was not included because of its smaller volume. Tissue samples were removed from formalin, frozen in liquid nitrogen, and freeze-dried. The brain material was subsequently pelleted and placed in the sample holder of a Superconducting Quantum Interference Device (SQUID) magnetometer.

Isothermal Remanent Magnetization (IRM) curves were acquired with a Quantum Design MPMS-XL SQUID magnetometer with the Reciprocating Sample Option probe, as reported previously (Bulk et al., 2018; Kumar et al., 2016), to explore whether the samples retained magnetization outside of an external magnetic field following stepwise exposure to higher magnetic field strengths at a constant temperature (Hautot et al., 2007, 2003). Two IRM curves were acquired: one at 5 K, which can report on ferrihydrite, the mineral found in the core of ferritin proteins and hemosiderin aggregates; and a second at 100 K, which saturated around 250 mT, indicative of magnetite or its oxidation product, maghemite. An example of the IRM curves for one of the samples is shown in Fig. 3. The IRM values were obtained after dividing the raw magnetic moment by the wet weight of the sample. Saturation IRM values (SIRM) were extracted by fitting the IRM curves to an offset-corrected Langevin model, as in our previous work (Bulk et al., 2018).

Ferrihydrite and maghemite concentrations were estimated by dividing the SIRM values by the saturation magnetization of the specific mineral: 0.62 Am^2/kg for ferrihydrite (Makhlouf et al., 1997), and 74 Am^2/kg for maghemite (Cao et al., 2016). Maghemite was chosen instead of magnetite, due to the high chance of sample oxidation during tissue processing. Subsequently, the ferrihydrite-iron and maghemite-iron concentrations were calculated by multiplying the mineral concentration by the iron mass-ratio for the given mineral. Concentrations of Fe^{3+}, ferrihydrite-iron and maghemite-iron that had been previously obtained under identical conditions from the temporal cortex of healthy controls are provided for comparison (Bulk et al., 2018).

Raw data post-processing of MRI, EPR and SQUID data was performed with an in-house written code in MatlabR2016a. Raw data obtained in this study are downloadable at the link: https://doi.org/10.17632/8b3fvc3h3f.1

3. Results

Table 1 provides an overview of all data collected from the aceruloplasminemia brain. The highest R_2* values were found in the lateral division of the thalamus and substantia nigra. On average, R_2* values within deep gray matter structures in aceruloplasminemia were over two times higher than those obtained from the temporal cortex. The deep gray matter structures in aceruloplasminemia had at least a three-fold increase in relaxation rates with respect to the close-by white matter, while in the temporal cortex the relative gray matter/white matter relaxation rate was reversed. Higher relaxation rates were observed in the white matter, which indicates a large fraction of iron being embedded in myelin. In the control subjects, both the white matter of the internal capsule and of the temporal lobe showed higher relaxation rates compared to the close-by gray matter (Fig. 4), but in all regions the relaxation rates were substantially lower than for the aceruloplasminemia case. Susceptibility values in aceruloplasminemia were only partially in accordance with the pattern of iron accumulation as suggested by the R_2* maps and were more heterogeneous within the structures (Fig. 4). Notable exceptions were the dentate nucleus, parts of the putamen and the temporal white matter, where a striking paramagnetic component was observed compared to close-by structures.

Ferrihydrite-iron was the most abundant form of iron in all investigated brain regions in aceruloplasminemia and represented 91–98% of all iron (Table 1). Mean concentrations of ferrihydrite-iron in the deep gray matter reached over 500 μg/g wet weight and were three times higher compared to the temporal cortex, which already exceeded the healthy situation by six times, on average. The amount of Fe^{3+} ions, detectable by EPR, and maghemite-iron in the temporal cortex of the patient with aceruloplasminemia was within the range of concentrations that had been detected in the control subjects. Although the ferrihydrite/maghemite-iron ratio was highly variable among structures, ferrihydrite-iron was at least three orders of magnitude more abundant than maghemite-iron, on average.

The distribution of Fe^{3+} ions and iron mineralization products in the aceruloplasminemia brain is visualized in Fig. 5. The globus pallidus and medial division of the thalamus, together with regions in the brain stem and cerebellum, showed the highest EPR-detectable Fe^{3+} concentration. The distribution of maghemite-iron appeared partially in accordance with this pattern, with the medial division of the thalamus, red nucleus, substantia nigra and dentate nucleus being the richest in this mineral form of iron. Maghemite levels in the lateral division of the thalamus and the putamen were below the detection limit of the technique.

4. Discussion

In this work, the iron-sensitive metrics R_2* and χ, obtained from 7 T MRI, were combined with Electron Paramagnetic Resonance (EPR) and SQUID magnetometry to specify and quantify the different iron forms in

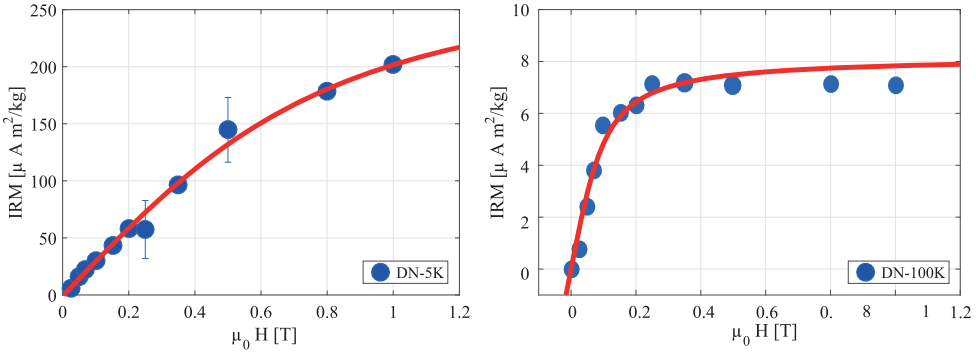

Fig. 3. Determination of ferrihydrite and maghemite by Isothermal Remanent Magnetization (IRM). IRM curves of the dentate nucleus (DN) at 5 K (left) and 100 K (right). The IRM curve at 100 K saturates around 0.25 T, which is a strong indication for the presence of magnetite or maghemite.

Table 1
Overview of MRI, EPR and SQUID results obtained from the aceruloplasminemia brain.

	7 T MRI		EPR		SQUID magnetometry				
Structure	**R_2*(ms^{-1})**	**χ(ppm)**	**Fe^{3+}(μg/g)**		**Ferrihydrite-iron** (μg/g)		**Maghemite-iron**(ng/g)		**Fh-iron**(%)
Red nucleus	0.3760	0.0033	24.15		1064.84		109.28		98
Thalamus L	0.4350	0.0103	15.00		709.72		UD		98
Caudate nucleus	0.2826	−0.0048	11.34		635.98		22.68		98
Dentate nucleus	0.3827	0.0501	20.88		319.58		90.27		94
Putamen	0.3254	0.0026	14.39		317.50		UD		96
Thalamus M	0.2118	−0.0474	28.62		290.01		259.07		91
Substantia nigra	0.4230	−0.0062	20.93		247.35		61.30		92
Temporal cortex	0.1400	−0.0124	9.21	*5.29 (2.0–10.0)*	161.68	*26.57 (7.24–39.31)*	23.40	*14.11(0–45.90)*	95
Globus pallidus	0.3338	−0.0014	34.06		NA		NA		–
White matter	0.1696	0.0565	8.12		175.43		13.77		96

R2* and χ results are shown as mean of the ROIs shown in Fig. 4. Concentrations are given per gram wet weight tissue, and previously obtained average (range) concentrations in the healthy brain (Bulk et al., 2018) are presented in italics. Abbreviations: Fh – ferrihydrite, M – medial division of the thalamus, L – lateral division of the thalamus, UD – undetectable, NA – not available.

the aceruloplasminemia brain. We detected and quantified ferrihydrite-iron – which is a measure of iron stores in the brain, maghemite-iron – an iron form that is recently attracting the attention of MR-physicists and biologists due to its potential neurotoxicity and the influence that it may have on MRI signal dephasing, and an EPR-sensitive pool of Fe^{3+} ions.

The comparison between R_2* and QSM maps indicated that a (para) magnetic source is driving the increase in relaxation rate in both gray and white matter structures in aceruloplasminemia. We ascribe this source to iron, mainly ferrihydrite-iron. The R_2* values showed that the lateral division of the thalamus, the substantia nigra, the dentate nucleus, and the red nucleus were heavily iron-loaded, which is in agreement with a recent *in vivo* study in aceruloplasminemia (Zhou et al., 2020). From the QSM maps, an increase in the paramagnetic signal was only observable in a few selected areas. Although QSM has the potential to more specifically identify the underlying source of R_2* increase, our reconstructions suffered from artefacts and the quality was not sufficient for quantitative analysis. These artefacts were likely caused by the large heterogeneity of iron accumulation within structures and the extremely short proton relaxation time as a result of the extremely high iron concentrations that impaired the detection of the signal. QSM reconstructions in aceruloplasminemia might therefore benefit from lower magnetic field strengths or shorter echo times, to partially mitigate these effects.

Of the three iron forms detected in the aceruloplasminemia brain, more than 90% was found to be associated with the ferritin storage protein and hemosiderin (ferrihydrite-iron). These findings agree with earlier histochemical studies of aceruloplasminemia brain tissue that showed the abundance of iron aggregates rich in Fe^{3+} that strongly reacted to ferritin light chain antibody (Kaneko et al., 2002, 2012), and observations in healthy brain tissue (Möller et al., 2019). The concentrations of ferrihydrite-iron in the basal ganglia of our patient with aceruloplasminemia could not be appropriately compared with results that had been previously obtained from the basal ganglia of healthy subjects and patients with neuroferritinopathy (Hautot et al., 2007), due to substantial methodological differences between studies. The amount of ferrihydrite-iron in the temporal cortex of aceruloplasminemia, though, was six times higher than in healthy subjects and almost four times higher compared to patients with advanced Alzheimer's disease that were measured under identical conditions, on average (Bulk et al., 2018; van der Weerd et al., 2020). Although these comparisons are limited to the temporal cortex, which is on average three times less rich in iron than the deep gray matter structures in aceruloplasminemia, they illustrate once more the severity of iron overload in the disease.

The distribution of ferrihydrite-iron throughout the brain in aceruloplasminemia did not reflect the total iron distribution in healthy brain tissue. While in normal ageing ferrihydrite-iron is most abundant in the globus pallidus and substantia nigra (Haacke et al., 2005), in this aceruloplasminemia brain very high levels of ferrihydrite-iron were detected in the red nucleus, caudate nucleus and thalamus. In addition, the thalamus showed a striking lateralization, with the lateral part being far more abundant in ferrihydrite-iron than the medial part of the structure. This may be explained by specific pathways that have been recently highlighted as possibly involved in iron transport between the caudate nucleus and the pulvinar nucleus within the lateral division of the thalamus (Zhou et al., 2020). The internal medullary lamina of the thalamus might additionally act as a barrier to prevent penetration of iron into the medial part of the structure (Kim et al., 2017). Although it should be noted that the globus pallidus was not assessed by magnetometry in this study, focal demyelination and iron accumulation with a preference for the pulvinar thalamus and caudate nucleus has also been described in patients with multiple sclerosis (Hagemeier et al., 2013; Haider et al., 2014), in which neurodegeneration and atrophy of these structures has been associated with disease progression and cognitive disturbances (Haider et al., 2014). Although this suggests a specific role of the caudate nucleus and (pulvinar) thalamus in neuroinflammation and neurodegeneration, different patterns of iron accumulation have been observed in Parkinson's disease, multiple system atrophy, progressive supranuclear palsy (Han et al., 2013), and other NBIA disorders (Kruer et al., 2012), of which the clinical relevance remains to be elucidated.

The above-mentioned lateralization within the thalamus, which was observed with quantitative MRI, EPR and SQUID magnetometry, is in accordance with previous *in vivo* MRI findings in aceruloplasminemia (Miyajima, 2015; Vroegindeweij et al., 2017; Kim et al., 2017). The relatively high R_2* values obtained from the lateral division of the thalamus appeared to be driven by the large amount of ferrihydrite-iron in this region, while the medial part of the thalamus showed a lower R_2* value despite being richer in maghemite-iron and EPR-detectable Fe^{3+} ions. Although the magnetization of maghemite is over two orders of magnitude higher compared to the one of ferrihydrite, its influence on iron-sensitive MRI remained limited due to the much lower concentration of maghemite nanocrystals compared to ferrihydrite (Dobson et al., 2009). Even though these observations do not exclude that ferrihydrite-iron and maghemite-iron may contribute together to the increase of tissue magnetic susceptibility, ferrihydrite-iron likely remains the main driver of MRI susceptibility contrast in extremely iron-loaded cases.

The potential role of maghemite-iron in the pathogenesis of aceruloplasminemia should not be discarded purely based on its limited contribution to the total brain iron pool. Absolute SIRM values detected at 100 K in aceruloplasminemia were approximately two orders of magnitude higher than those reported in healthy subjects, at room temperature (Gilder et al., 2018), which suggests that also maghemite-iron levels may have increased as a result of iron overload in aceruloplasminemia. On the other hand, the concentration of maghemite-iron detected in the temporal cortex of aceruloplasminemia was not increased compared to healthy controls and advanced cases of

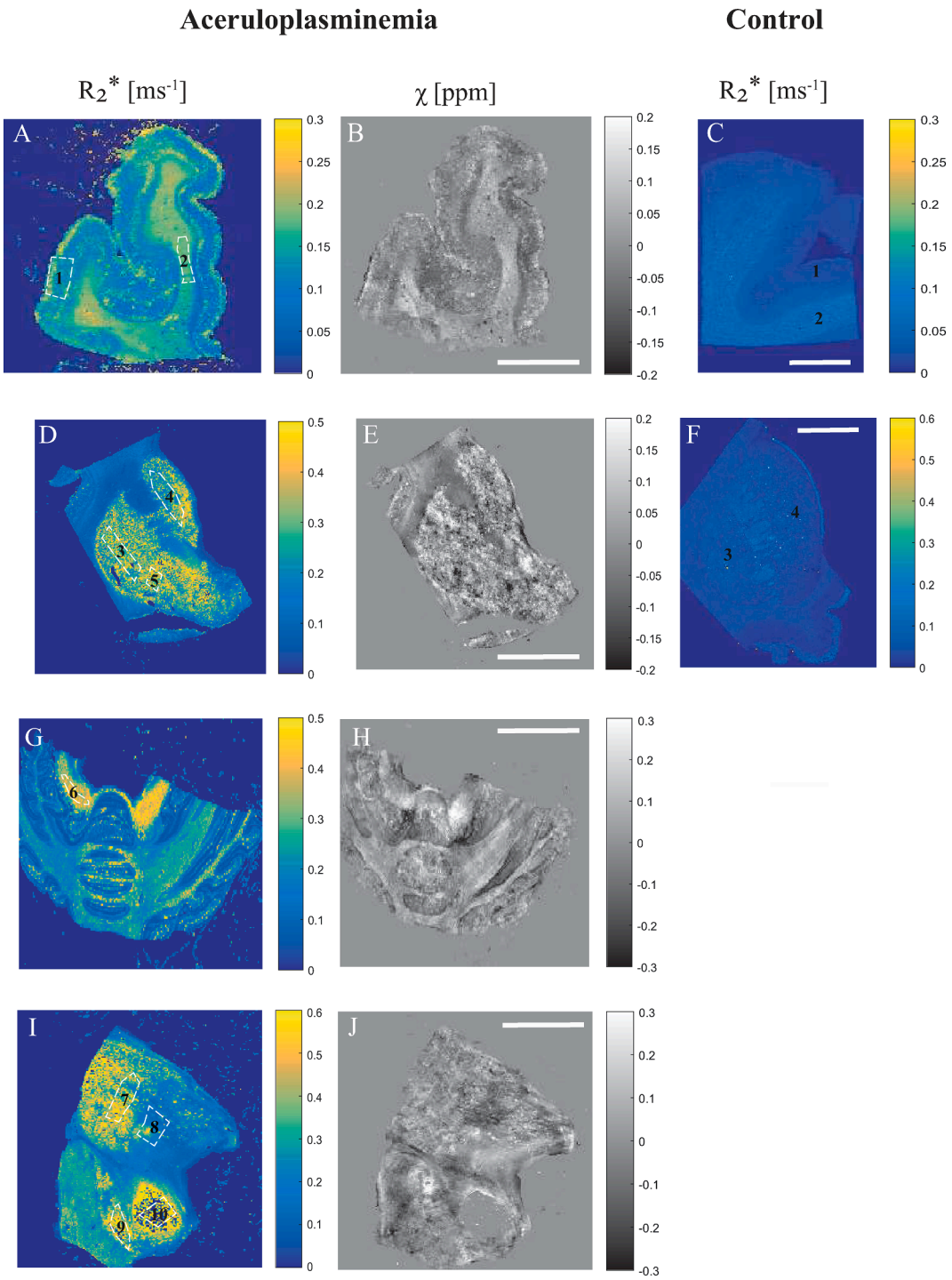

Fig. 4. Comparison of quantitative MRI results. The R_2* and QSM maps are shown with the outlined regions of interest (ROIs) in the temporal cortex (1) and white matter (2) (A, B), putamen (3), caudate nucleus (4) and globus pallidus (5) (D, E), dentate nucleus (6) (G, H), thalamus (7–ateral division,8–medial division), substantia nigra (9) and red nucleus (10) (I, J) in aceruloplasminemia. Note that for the red nucleus, the susceptibility signal was predominantly masked out (J). R_2* maps of the temporal cortex (1) and white matter (2) (C), putamen (3) and caudate nucleus (4)(F) of a control subject are provided for comparison. Scalebar, 1 cm. (For interpretation of the references to colour in this figure legend, the reader is referred to the web version of this article.)

Alzheimer's disease that were measured under identical conditions (Bulk et al., 2018; van der Weerd et al., 2020). In addition, in contrast to ferrihydrite-iron, the regional distribution of maghemite-iron in the aceruloplasminemia brain was not substantially different from that of healthy controls (Gilder et al., 2018), with the cerebellar and brain stem nuclei being relatively rich in this magnetic carrier, although thalamic structures were not specifically investigated by previous studies (Gilder et al., 2018). The preserved distribution of maghemite-iron throughout the severely diseased aceruloplasminemia brain rather questions its biological relevance, which has already been a subject of debate in other iron-related neurodegenerative conditions (Bulk et al., 2018; Kumar et al., 2016; Hautot et al., 2007, 2003; Pankhurst et al., 2008). Being able to distinguish between the contribution of ferrihydrite-iron and maghemite-iron to MRI contrast *in vivo* is important to unravel a possible cause-effect relationship between the amount of maghemite-iron and the severity of neurological manifestations, which might shed new light

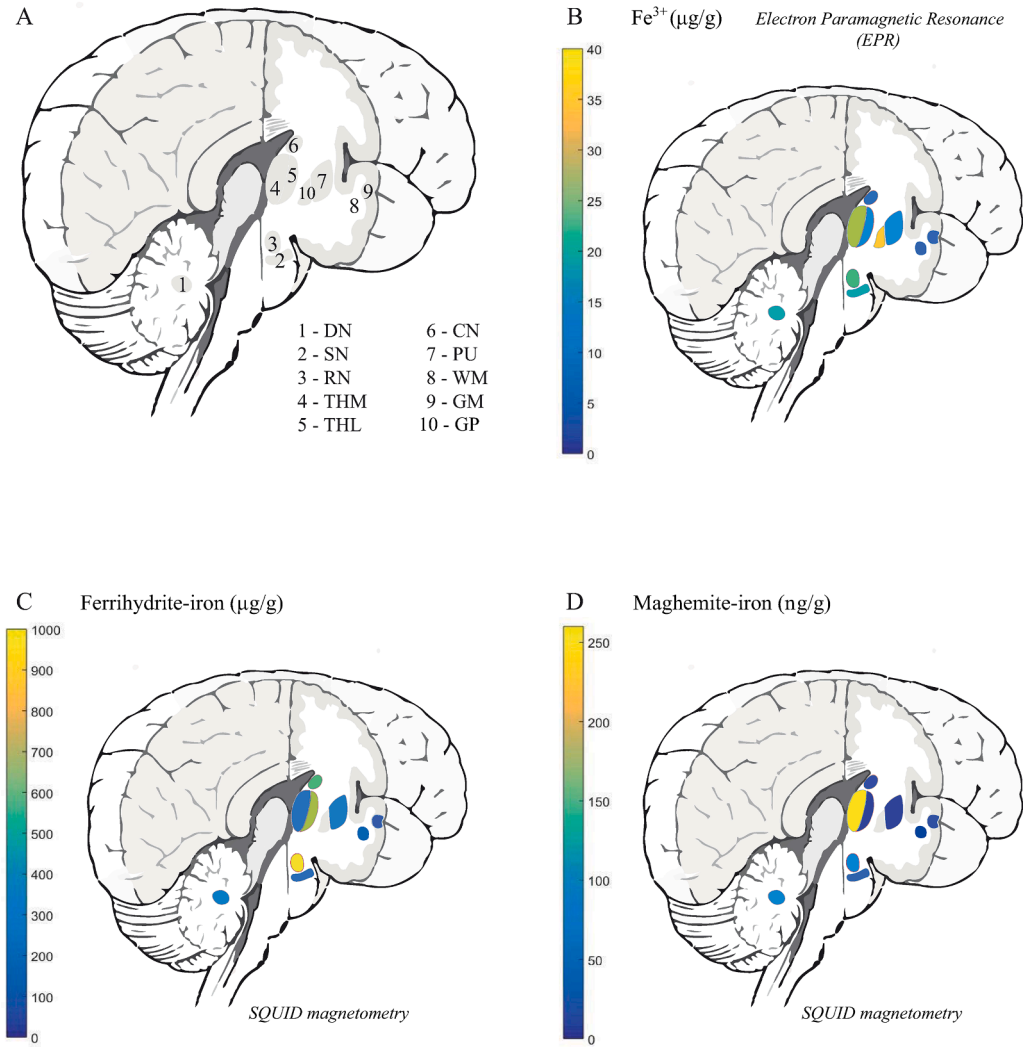

Fig. 5. Distribution of different iron forms in aceruloplasminemia brain tissue. Abbreviations: DN – dentate nucleus, SN – substantia nigra, RN – red nucleus, THM – medial division of the thalamus, THL – lateral division of the thalamus, CN – caudate nucleus, GP – globus pallidus, PU – putamen, WM – white matter, GM – gray matter. (For interpretation of the references to colour in this figure legend, the reader is referred to the web version of this article.)

on the pathophysiological role of maghemite-iron in iron-related neurodegeneration.

The EPR-detected Fe^{3+} ions are complementary to the two above-mentioned iron forms and may account for a part of the labile iron pool, which is implicated in the formation of reactive oxygen species and for monomeric iron sites in the ferritin shell that are responsible for ferroxidase activity. Although EPR also has the potential to detect ferrihydrite-iron and maghemite-iron, the signal from these minerals is optimal at higher temperatures than used here (Wajnberg et al., 2001), and would require a much larger sample mass than what employed by us. Given its low abundance and relatively small magnetic moment, it is unlikely that Fe^{3+} ions significantly affect the MRI signal in aceruloplasminemia.

Our work has some limitations, the first being the long-term formalin fixation of the tissue. Since formalin fixation is known to reduce total tissue iron content and may have a detrimental effect on protein conformations (Schrag et al., 2010; Gellein et al., 2008; Ghosh et al., 2010; Kalyanaraman et al., 2019), it is likely that the presented absolute concentrations of Fe^{3+} ions, ferrihydrite-iron and maghemite-iron in the aceruloplasminemia brain are underestimated compared to *in vivo*. In addition, formalin fixation has likely increased the R_2* values, compared to *in vivo* conditions (Birkl et al., 2016). Therefore, future studies should aim to minimize the duration of formalin fixation (van der Weerd et al., 2020), and ideally include both aceruloplasminemia and control brain tissue to enable more in-depth analyses of the exact relationship between the different molecular forms of iron that are present in healthy and severely diseased states. On the other hand, the spatial distribution of the different iron forms, as presented in our work, is not significantly affected by prolonged formalin fixation (Gilder et al., 2018). This is confirmed by the non-uniform distribution of iron within the thalamus in our study, which is in accordance with previous *in vivo* MRI findings in aceruloplasminemia (Miyajima, 2015; Vroegindeweij et al., 2017; Kim et al., 2017). Given the short T_2* values that characterize the aceruloplasminemia brain, future studies should additionally aim to employ data acquisition techniques that allow a shorter first echo-time and inter-echo spacing, e. g. radial k-space coverage. The lack of T_2 maps represents another limitation of our current work, since spin-echo decay could add valuable information on the degree of iron aggregation e.g. in the form of hemosiderin (Jensen et al., 2010), and the ratio between R_2* and R_2 could reveal important information on the effective size of the iron-rich compartments (Lee et al., 2018). Moreover, the reported ferrihydrite-iron and maghemite-iron concentrations should be considered as approximate rather than absolute values, given the assumptions that had to be made to obtain these iron concentrations from the SIRM values. However, we believe that reporting iron concentrations instead of SIRM values can help guiding the interpretation of the results in the

context of biology. Finally, since our results are based on a single patient study, generalization to other cases should be done carefully. It should be noted, though, that the rarity of aceruloplasminemia makes the tissue availability a challenge, as illustrated by the fact that only six other autopsy cases have been published over decades (Morita et al., 1995; Kaneko et al., 2002, 2012; Kawanami et al., 1996).

In conclusion, ferrihydrite-iron is the major determinant of iron-sensitive MRI contrast, and is the most abundant iron form in the aceruloplasminemia brain. Among the studied regions, the lateral division of the thalamus, the red nucleus and the basal ganglia contained the highest amounts of ferrihydrite-iron. The maintenance of ferritin as the major iron storing protein in extremely iron-loaded brain tissue, as observed in our study, has major implications for the concept of iron chelation as the main treatment for aceruloplasminemia and other NBIA disorders. In particular, deferiprone is currently being exploited to treat several NBIA diseases (Vroegindeweij et al., 2020; Klopstock et al., 2019). Deferiprone is the only iron chelator known to date that is capable of transporting iron across cell membranes and across the blood brain barrier. As it selectively binds Fe^{3+} and is capable of directly removing Fe^{3+} ions from the core of ferritin (Bou-Abdallah et al., 2011), our findings pathophysiologically support the clinical benefit of deferiprone that has been reported in patients with aceruloplasminemia and other NBIA disorders (Vroegindeweij et al., 2020; Klopstock et al., 2019), and highlight the potential of specifically quantifying ferrihydrite-iron *in vivo* to improve the use of iron-sensitive MRI metrics as an outcome measure of iron chelation therapy.

CRediT authorship contribution statement

Lena H.P. Vroegindeweij: Conceptualization, Methodology, Resources, Writing - original draft, Visualization, Project administration. **Lucia Bossoni:** Methodology, Software, Investigation, Writing - original draft, Visualization, Project administration. **Agnita J.W. Boon:** Conceptualization, Writing - review & editing. **J.H. Paul Wilson:** Conceptualization, Writing - review & editing. **Marjolein Bulk:** Resources, Writing - review & editing. **Jacqueline Labra-Muñoz:** Resources, Investigation, Writing - review & editing. **Martina Huber:** Resources, Writing - review & editing. **Andrew Webb:** Resources, Writing - review & editing. **Louise van der Weerd:** Methodology, Writing - review & editing, Supervision. **Janneke G. Langendonk:** Conceptualization, Methodology, Writing - review & editing, Supervision.

Declaration of Competing Interest

The authors declare that they have no known competing financial interests or personal relationships that could have appeared to influence the work reported in this paper.

Acknowledgements

The authors are very grateful to the patient with aceruloplasminemia and his family to agree with this research, would like to thank A. Lefering for access to the SQUID and technical assistance, and S.A. Bonnet and S. Zheng for access to the ICP-MS and measuring the iron concentration of the formalin solution.

Ethical approval

This study was approved by the Medical Ethics Review Board of the Erasmus MC (approval number: MEC-2011-525).

Funding

This study was supported by the Dutch Foundation for Fundamental Research on Matter (FOM), by the Netherlands Organization for Scientific Research (NWO) through a VENI fellowship to L.B. (0.16.Veni.188.040), and a grant from the ZonMw program Innovative Medical Devices Initiative, project Imaging Dementia: Brain Matters (104003005) to M.B. M.H. and J. L.-M. are founded by the NWO Zwartekrachtprogram, Nanofront project NF17SYN05.

Appendix A. Supplementary data

Supplementary data to this article can be found online at https://doi.org/10.1016/j.nicl.2021.102657.

References

Miyajima, H., Takahashi, Y., Kono, S., 2003. Aceruloplasminemia, an inherited disorder of iron metabolism. Biometals 16 (1), 205–213.
Miyajima, H., 2015. Aceruloplasminemia. Neuropathology 35 (1), 83–90.
Morita, H., Ikeda, S.-I., Yamamoto, K., Morita, S., Yoshida, K., Nomoto, S., Kato, M., Yanagisawa, N., 1995. Hereditary ceruloplasmin deficiency with hemosiderosis: a clinicopathological study of a Japanese family. Ann Neurol. 37 (5), 646–656.
Miyajima, H., 2015. Investigated and available therapeutic options for treating aceruloplasminemia. Expert Opin. Orphan Drugs 3 (9), 1011–1020.
Sassi, M., Rosso, K.M., 2019. Roles of Hydration and Magnetism on the Structure of Ferrihydrite from First Principles. ACS Earth Space Chem. 3 (1), 70–78.
Dobson, J., 2001. Nanoscale biogenic iron oxides and neurodegenerative disease. FEBS Lett. 496 (1), 1–5.
Markesbery, W.R., 1997. Oxidative stress hypothesis in Alzheimer's disease. Free Radic Biol Med. 23 (1), 134–147.
Kirschvink, J.L., Kobayashi-Kirschvink, A., Woodford, B.J., 1992. Magnetite biomineralization in the human brain. Proc. Natl. Acad. Sci. U.S.A. 89 (16), 7683–7687.
Kaneko, K., Yoshida, K., Arima, K., Ohara, S., Miyajima, H., Kato, T., Ohta, M., Ikeda, S.-I., 2002. Astrocytic deformity and globular structures are characteristic of the brains of patients with aceruloplasminemia. J. Neuropathol. Exp Neurol. 61 (12), 1069–1077.
Kaneko, K., Hineno, A., Yoshida, K., Ohara, S., Morita, H., Ikeda, S.-I., 2012. Extensive brain pathology in a patient with aceruloplasminemia with a prolonged duration of illness. Hum. Pathol. 43 (3), 451–456.
Gonzalez-Cuyar LF, Perry G, Miyajima H, Atwood CS, Riveros-Angel M, Lyons PF, et al. Redox active iron accumulation in aceruloplasminemia. Neuropathology. 2008;28 (5):466-71.
Haacke, E.M., Cheng, N.Y.C., House, M.J., Liu, Q., Neelavalli, J., Ogg, R.J., Khan, A., Ayaz, M., Kirsch, W., Obenaus, A., 2005. Imaging iron stores in the brain using magnetic resonance imaging. Magn. Reson. Imaging. 23 (1), 1–25.
Dusek, P., Dezortova, M., Wuerfel, J., 2013. Imaging of iron. Int. Rev. Neurobiol. 110, 195–239.
Cherubini, A., Péran, P., Hagberg, G.E., Varsi, A.E., Luccichenti, G., Caltagirone, C., Sabatini, U., Spalletta, G., 2009. Characterization of white matter fiber bundles with T2* relaxometry and diffusion tensor imaging. Magn. Reson. Med. 61 (5), 1066–1072.
Wharton, S., Bowtell, R., 2012. Fiber orientation-dependent white matter contrast in gradient echo MRI. Proc. Natl. Acad. Sci. 109 (45), 18559–18564.
Stüber, C., Morawski, M., Schäfer, A., Labadie, C., Wähnert, M., Leuze, C., Streicher, M., Barapatre, N., Reimann, K., Geyer, S., Spemann, D., Turner, R., 2014. Myelin and iron concentration in the human brain: a quantitative study of MRI contrast. Neuroimage. 93, 95–106.
Gong, N.-J., Dibb, R., Bulk, M., van der Weerd, L., Liu, C., 2019. Imaging beta amyloid aggregation and iron accumulation in Alzheimer's disease using quantitative susceptibility mapping MRI. Neuroimage. 191, 176–185.
Colgan, T.J., Knobloch, G., Reeder, S.B., Hernando, D., 2020. Sensitivity of quantitative relaxometry and susceptibility mapping to microscopic iron distribution. Magn Reson Med. 83 (2), 673–680.
Pan, P.-L., Tang, H.-H., Chen, Q., Song, W., Shang, H.-F., 2011. Desferrioxamine treatment of aceruloplasminemia: Long-term follow-up. Mov Disord. 26 (11), 2142–2144.
Zhou, L., Chen, Y., Li, Y., Gharabaghi, S., Chen, Y., Sethi, S.K., Wu, Y., Haacke, E.M., 2020. Intracranial iron distribution and quantification in aceruloplasminemia: A case study. Magn Reson Imaging. 70, 29–35.
Bulk, M., van der Weerd, L., Breimer, W., Lebedev, N., Webb, A., Goeman, J.J., Ward, R. J., Huber, M., Oosterkamp, T.H., Bossoni, L., 2018. Quantitative comparison of different iron forms in the temporal cortex of Alzheimer patients and control subjects. Sci Rep. 8 (1) https://doi.org/10.1038/s41598-018-25021-7.
Vroegindeweij, L.H.P., van der Beek, E.H., Boon, A.J.W., Hoogendoorn, M., Kievit, J.A., Wilson, J.H.P., Langendonk, J.G., 2015. Aceruloplasminemia presents as Type 1 diabetes in non-obese adults: a detailed case series. Diabet Med. 32 (8), 993–1000.
Vroegindeweij, L.H.P., Langendonk, J.G., Langeveld, M., Hoogendoorn, M., Kievit, A.J. A., Di Raimondo, D., Wilson, J.H.P., Boon, A.J.W., 2017. New insights in the neurological phenotype of aceruloplasminemia in Caucasian patients. Parkinsonism Relat Disord. 36, 33–40.
Kerkhof, M., Honkoop, P., 2014. Never forget aceruloplasminemia in case of highly suggestive Wilson's disease score. Hepatology 59 (4), 1645–1647.

Vroegindeweij, L.H.P., Boon, A.J.W., Wilson, J.H.P., Langendonk, J.G., 2020. Effects of iron chelation therapy on the clinical course of aceruloplasminemia: an analysis of aggregated case reports. Orphanet J. Rare Diseas. 15 (1), 105.

Shepherd, T.M., Thelwall, P.E., Stanisz, G.J., Blackband, S.J., 2009. Aldehyde fixative solutions alter the water relaxation and diffusion properties of nervous tissue. Magn Reson Med. 62 (1), 26–34.

Bouhrara, M., Reiter, D.A., Celik, H., Bonny, J.-M., Lukas, V., Fishbein, K.W., Spencer, R. G., 2015. Incorporation of Rician noise in the analysis of biexponential transverse relaxation in cartilage using a multiple gradient echo sequence at 3 and 7 Tesla. Magn Reson Med. 73 (1), 352–366.

Li, W., Avram, A.V., Wu, B., Xiao, X., Liu, C., 2014. Integrated Laplacian-based phase unwrapping and background phase removal for quantitative susceptibility mapping. NMR Biomed. 27 (2), 219–227.

Li W, Wu B, Liu C. iHARPERELLA: an improved method for integrated 3D phase unwrapping and background phase removal [Abstract]. In: Proceedings of the 23rd Annual Meeting & Exhibition ISMRM, 30 May-5 June 2015; Toronto, Ontario, Canada. Available from: http://archive.ismrm.org/2015/3313.html [accessed 7 April 2020].

Li, W., Wang, N., Yu, F., Han, H., Cao, W., Romero, R., Tantiwongkosi, B., Duong, T.Q., Liu, C., 2015. A method for estimating and removing streaking artifacts in quantitative susceptibility mapping. Neuroimage. 108, 111–122.

Bulk, M., Kenkhuis, B., van der Graaf, L.M., Goeman, J.J., Natté, R., van der Weerd, L., Bush, A., 2018. Postmortem T 2 *- Weighted MRI Imaging of Cortical Iron Reflects Severity of Alzheimer's Disease. J. Alzheimers Dis. 65 (4), 1125–1137.

Kumar, P., Bulk, M., Webb, A., van der Weerd, L., Oosterkamp, T.H., Huber, M., Bossoni, L., 2016. A novel approach to quantify different iron forms in ex-vivo human brain tissue. Sci Rep. 6 (1) https://doi.org/10.1038/srep38916.

Stoll, S., Schweiger, A., 2006. EasySpin, a comprehensive software package for spectral simulation and analysis in EPR. J Magn Reson. 178 (1), 42–55.

Hautot, D., Pankhurst, Q.A., Morris, C.M., Curtis, A., Burn, J., Dobson, J., 2007. Preliminary observation of elevated levels of nanocrystalline iron oxide in the basal ganglia of neuroferritinopathy patients. BBA 1772 (1), 21–25.

Hautot, D., Pankhurst, Q.A., Khan, N., Dobson, J., 2003. Preliminary evaluation of nanoscale biogenic magnetite in Alzheimer's disease brain tissue. Proc Biol Sci. 270 (Suppl 1), S62–S64.

Makhlouf, S.A., Parker, F.T., Berkowitz, A.E., 1997. Magnetic hysteresis anomalies in ferritin. Physical Review B. 55 (22), R14717–R14720.

Cao, D., Li, H., Pan, L., Li, J., Wang, X., Jing, P., et al., 2016. High saturation magnetization of gamma-Fe2O3 nano-particles by a facile one-step synthesis approach. Sci Rep. 6, 32360.

Möller, H.E., Bossoni, L., Connor, J.R., Crichton, R.R., Does, M.D., Ward, R.J., Zecca, L., Zucca, F.A., Ronen, I., 2019. Iron, Myelin, and the Brain: Neuroimaging Meets Neurobiology. Trends Neurosci. 42 (6), 384–401.

van der Weerd, L., Lefering, A., Webb, A., Egli, R., Bossoni, L., 2020. Effects of Alzheimer's disease and formalin fixation on the different mineralised-iron forms in the human brain. Sci. Rep. 10 (1), 16440.

Kim, H.K., Ki, C.S., Kim, Y.J., Lee, M.S., 2017. Radiological Findings of Two Sisters with Aceruloplasminemia Presenting with Chorea. Clinical neuroradiology. 27 (3), 385–388.

Hagemeier, J., Yeh, E.A., Brown, M.H., Bergsland, N., Dwyer, M.G., Carl, E., Weinstock-Guttman, B., Zivadinov, R., 2013. Iron content of the pulvinar nucleus of the thalamus is increased in adolescent multiple sclerosis. Multiple Sclerosis J. 19 (5), 567–576.

Haider, L., Simeonidou, C., Steinberger, G., Hametner, S., Grigoriadis, N., Deretzi, G., Kovacs, G.G., Kutzelnigg, A., Lassmann, H., Frischer, J.M., 2014. Multiple sclerosis deep grey matter: the relation between demyelination, neurodegeneration, inflammation and iron. J Neurol Neurosurg Psychiatry. 85 (12), 1386–1395.

Han, Y.-H., Lee, J.-H., Kang, B.-M., Mun, C.-W., Baik, S.-K., Shin, Y.-i., Park, K.-H., 2013. Topographical differences of brain iron deposition between progressive supranuclear palsy and parkinsonian variant multiple system atrophy. J. Neurol. Sci. 325 (1-2), 29–35.

Kruer, M.C., Boddaert, N., Schneider, S.A., Houlden, H., Bhatia, K.P., Gregory, A., Anderson, J.C., Rooney, W.D., Hogarth, P., Hayflick, S.J., 2012. Neuroimaging features of neurodegeneration with brain iron accumulation. AJNR Am J Neuroradiol. 33 (3), 407–414.

Dobson, J., Bowtell, R., Garcia-Prieto, A., Pankhurst, Q., Sokolov, I., 2009. Safety implications of high-field MRI: actuation of endogenous magnetic iron oxides in the human body. PLoS ONE 4 (5), e5431. https://doi.org/10.1371/journal.pone.000543110.1371/journal.pone.0005431.g00110.1371/journal.pone.0005431.g002.

Gilder, S.A., Wack, M., Kaub, L., Roud, S.C., Petersen, N., Heinsen, H., Hillenbrand, P., Milz, S., Schmitz, C., 2018. Distribution of magnetic remanence carriers in the human brain. Sci Rep. 8 (1) https://doi.org/10.1038/s41598-018-29766-z.

Pankhurst, Q., Hautot, D., Khan, N., Dobson, J., 2008. Increased levels of magnetic iron compounds in Alzheimer's disease. J Alzheimers Dis. 13 (1), 49–52.

Wajnberg E, El-Jaick LJ, Linhares MP, Esquivel DM. Ferromagnetic resonance of horse spleen ferritin: core blocking and surface ordering temperatures. Journal of magnetic resonance (San Diego, Calif : 1997). 2001;153(1):69-74.

Schrag, M., Dickson, A., Jiffry, A., Kirsch, D., Vinters, H.V., Kirsch, W., 2010. The effect of formalin fixation on the levels of brain transition metals in archived samples. Biometals 23 (6), 1123–1127.

Gellein, K., Flaten, T.P., Erikson, K.M., Aschner, M., Syversen, T., 2008. Leaching of trace elements from biological tissue by formalin fixation. Biol Trace Elem Res. 121 (3), 221–225.

Ghosh, A., Chandran, K., Kalivendi, S.V., Joseph, J., Antholine, W.E., Hillard, C.J., Kanthasamy, A., Kanthasamy, A., Kalyanaraman, B., 2010. Neuroprotection by a mitochondria-targeted drug in a Parkinson's disease model. Free Radical Biol. Med. 49 (11), 1674–1684.

Kalyanaraman, B., Cheng, G., Zielonka, J., Bennett, B., 2019. Low-Temperature EPR Spectroscopy as a Probe-Free Technique for Monitoring Oxidants Formed in Tumor Cells and Tissues: Implications in Drug Resistance and OXPHOS-Targeted Therapies. Cell Biochem. Biophys. 77 (1), 89–98.

Birkl, C., Langkammer, C., Golob-Schwarzl, N., Leoni, M., Haybaeck, J., Goessler, W., Fazekas, F., Ropele, S., 2016. Effects of formalin fixation and temperature on MR relaxation times in the human brain. NMR Biomed. 29 (4), 458–465.

Jensen, J.H., Tang, H., Tosti, C.L., Swaminathan, S.V., Nunez, A., Hultman, K., Szulc, K. U., Wu, E.X., Kim, D., Sheth, S., Brown, T.R., Brittenham, G.M., 2010. Separate MRI quantification of dispersed (ferritin-like) and aggregated (hemosiderin-like) storage iron. Magn. Reson. Med. 63 (5), 1201–1209.

Lee, H., Baek, S.-Y., Chun, S.Y., Lee, J.-H., Cho, HyungJoon, 2018. Specific visualization of neuromelanin-iron complex and ferric iron in the human post-mortem substantia nigra using MR relaxometry at 7T. NeuroImage. 172, 874–885.

Kawanami, T., Kato, T., Daimon, M., Tominaga, M., Sasaki, H., Maeda, K., Arai, S., Shikama, Y., Katagiri, T., 1996. Hereditary caeruloplasmin deficiency: clinicopathological study of a patient. J Neurol Neurosurg Psychiatry. 61 (5), 506–509.

Klopstock, T., Tricta, F., Neumayr, L., Karin, I., Zorzi, G., Fradette, C., Kmieć, T., Büchner, B., Steele, H.E., Horvath, R., Chinnery, P.F., Basu, A., Küpper, C., Neuhofer, C., Kálmán, B., Dušek, P., Yapici, Z., Wilson, I., Zhao, F., Zibordi, F., Nardocci, N., Aguilar, C., Hayflick, S.J., Spino, M., Blamire, A.M., Hogarth, P., Vichinsky, E., 2019. Safety and efficacy of deferiprone for pantothenate kinase-associated neurodegeneration: a randomised, double-blind, controlled trial and an open-label extension study. Lancet Neurol. 18 (7), 631–642.

Bou-Abdallah, F., McNally, J., Liu, X.X., Melman, A., 2011. Oxygen catalyzed mobilization of iron from ferritin by iron(III) chelate ligands. Chem. Commun. (Camb.) 47 (2), 731–733.